

# Structural Understanding of Superior Battery Properties of Partially Ni-Doped $\text{Li}_2\text{MnO}_3$ as Cathode Material

Toshiyuki Matsunaga,<sup>\*,†</sup> Hideyuki Komatsu,<sup>†</sup> Keiji Shimoda,<sup>†</sup> Taketoshi Minato,<sup>†</sup> Masao Yonemura,<sup>‡</sup> Takashi Kamiyama,<sup>‡</sup> Shunsuke Kobayashi,<sup>§</sup> Takeharu Kato,<sup>§</sup> Tsukasa Hirayama,<sup>§,||</sup> Yuichi Ikuhara,<sup>§,||</sup> Hajime Arai,<sup>†</sup> Yoshio Ukyo,<sup>†</sup> Yoshiharu Uchimoto,<sup>⊥</sup> and Zempachi Ogumi<sup>†</sup>

<sup>†</sup>Office of Society-Academia Collaboration for Innovation, Kyoto University, Gokasho, Uji, Kyoto 611-0011, Japan

<sup>‡</sup>Neutron Science Laboratory, Institute of Materials Structure Science, High Energy Accelerator Research Organization, 1-1 Oho, Tsukuba, Ibaraki 305-0801, Japan

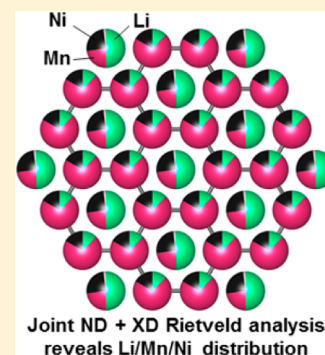
<sup>§</sup>Nanostructures Research Laboratory, Japan Fine Ceramics Center, 2-4-1 Mutsuno, Atsuta, Nagoya 456-8587, Japan

<sup>||</sup>Institute of Engineering Innovation, University of Tokyo, 2-11-16 Yayoi, Bunkyo-ku, Tokyo 113-8656, Japan

<sup>⊥</sup>Graduate School of Human and Environmental Studies, Kyoto University, Yoshida-nihonmatsu-cho, Sakyo-ku, Kyoto 606-8501, Japan

## Supporting Information

**ABSTRACT:** We examined the crystal structures of  $\text{Li}_2(\text{Ni}_x\text{Mn}_{1-x})\text{O}_3$  ( $x = 0, 1/10, 1/6$ , and  $1/4$ ) to elucidate the relationship between the structure and electrochemical performance of the compounds using neutron and synchrotron X-ray powder diffraction analyses in combination. Our examination revealed that these crystals contain a large number of stacking faults and exhibit significant cation mixing in the transition-metal layers; the cation mixing becomes significant with an increase in the Ni concentration. Charge–discharge measurements showed that the replacement of Mn with Ni lowers the potential of the charge plateau and leads to higher charge–discharge capacities. From a topological point of view with regard to the atomic arrangement in the crystals, it is concluded that substituting Mn in  $\text{Li}_2\text{MnO}_3$  with Ni promotes the formation of smooth Li percolation paths, thus increasing the number of active Li ions and improving the charge–discharge capacity.



In recent years, so-called Li-rich compounds  $\text{Li}_2\text{MO}_3$  [ $\text{Li}(\text{Li}_{1/3}\text{M}_{2/3})\text{O}_2$ ; M: transition metal (TM)] have been investigated for use as cathode materials in lithium-ion batteries because they show specific capacities ( $200 \text{ mA h g}^{-1}$ ) higher than those of  $\text{LiMO}_2$ . Among the various  $\text{Li}_2\text{MO}_3$  compounds being explored,  $\text{Li}_2\text{MnO}_3$  has been examined particularly intensively.<sup>1–3</sup> On the other hand, about a decade ago, Lu et al. investigated the structures and battery properties of  $\text{Li}[\text{Ni}_x\text{Li}_{1/3-2x/3}\text{Mn}_{2/3-x/3}]\text{O}_2$  materials, which are solid solutions of  $\text{Li}(\text{Li}_{1/3}\text{Mn}_{2/3})\text{O}_2$  [ $\text{Li}_2\text{MnO}_3$ ], and  $\text{Li}(\text{Ni}_{1/2}\text{Mn}_{1/2})\text{O}_2$  ( $1-2x: 2x$ ; see Supporting Information, Figure S-1) and found that they show better electrochemical performances than does  $\text{Li}(\text{Li}_{1/3}\text{Mn}_{2/3})\text{O}_2$ , especially at  $x = 1/3$  to  $5/12$ .<sup>4</sup> In addition to this study, other efforts have also been made to improve the performance of such Li-rich materials.<sup>5</sup> Recently, the combined use of X-ray and neutron diffraction analyses allowed us to determine the structural parameters of such complex crystals with precision. In addition, to analyze the structural defects, the FAULTS program created by Casas-Cabanas<sup>6</sup> et al. is helpful because it simultaneously allows for Rietveld refinement and stacking fault analysis based on DIFFaX.<sup>7</sup>

In this study, we prepared five  $\text{Li}_2(\text{Ni}_x\text{Mn}_{1-x})\text{O}_3$  ( $x = 0, 1/20, 1/10, 1/6$ , and  $1/4$ ) specimens and scrutinized their structures as well as with their structural defects complementarily using a general Rietveld program, Z-Rietveld<sup>8</sup> (for the

joint analysis), and the FAULTS program (for the stacking fault analysis). The results of quantitative analysis for these five specimens are listed in Table S-I. It was assumed that the metal atomic sites (Li and TM layers in the  $\text{Li}_2\text{MnO}_3$  structure; see below for structural details) are all filled with atoms, that is, they do not have any vacancies. We prepared the starting materials so as to form  $\text{Li}_2(\text{Ni}_x\text{Mn}_{1-x})\text{O}_3$  pseudobinary compounds; however, as can be seen from Table S-I and Figure S-1, the resultant materials were formed away from the  $\text{Li}_2\text{MnO}_3$ – $\text{Li}_2\text{NiO}_3$  pseudobinary line.

Figure 1 shows the first cycle charge–discharge profiles of the  $\text{Li}_2(\text{Ni}_x\text{Mn}_{1-x})\text{O}_3$  ( $x = 0, 1/20, 1/10$ , and  $1/4$ ) specimens. As can be seen in Figure 1, their specific capacities are not sufficiently high; however, the dependence of the specific capacity on the Ni composition is almost similar to that reported by Beaulieu<sup>4,9</sup> et al., which is that replacing Mn with Ni lowers the potential of the charge plateau and leads to higher charge–discharge capacities.

Figure 2 shows the synchrotron diffraction patterns obtained for the four  $\text{Li}_2(\text{Ni}_x\text{Mn}_{1-x})\text{O}_3$  ( $x = 0, 1/10, 1/6$ , and  $1/4$ ) materials. The diffraction patterns are almost similar, suggesting

Received: March 14, 2016

Accepted: May 16, 2016

Published: May 19, 2016



that the pseudobinary compounds are all isostructural with  $\text{Li}_2\text{MnO}_3$ .  $\text{Li}_2\text{MnO}_3$  is known, as shown in Figure S-2, to have a monoclinic structure (space group  $C2/m$ ) consisting of three

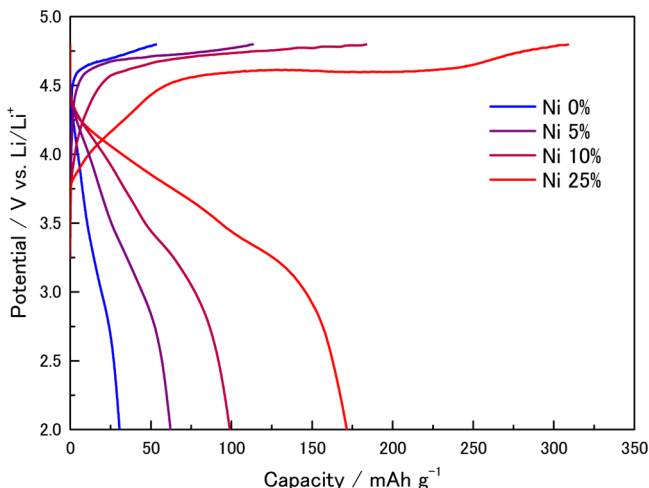


**Figure 1.** First charge–discharge curves of  $\text{Li}_2(\text{Ni}_x\text{Mn}_{1-x})\text{O}_{3(-\delta)}$  ( $x = 0, 1/20, 1/10$ , and  $1/4$ ) between 2.0 and 4.8 V (vs  $\text{Li}/\text{Li}^+$ ) at a rate of  $10 \text{ mA g}^{-1}$  as measured at room temperature.

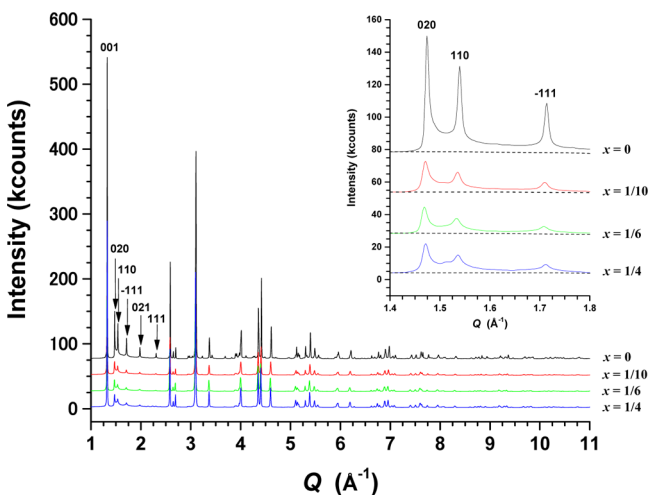
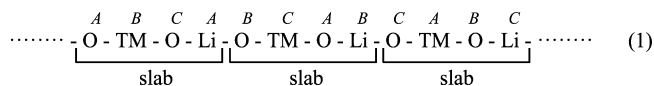


**Figure 2.** Synchrotron diffraction patterns of  $\text{Li}_2(\text{Ni}_x\text{Mn}_{1-x})\text{O}_{3(-\delta)}$  ( $x = 0, 1/10, 1/6$ , and  $1/4$ ). The arrows indicate the positions of the 020, 110,  $\bar{1}11$ , 021, and 111 superstructure reflections. The insets show magnified images of the low-angle parts; fairly intense diffuse peaks from the stacking faults can be seen, especially at the bottoms of the 020, 110, and  $\bar{1}11$  superstructure reflections (the background profiles are represented by the broken lines). These superstructure reflections appear to consist of diffuse peaks and sharp Bragg peaks, suggesting that the four  $\text{Li}_2(\text{Ni}_x\text{Mn}_{1-x})\text{O}_{3(-\delta)}$  compounds were composed of two kinds of domains with different crystallinities. During the subsequent two-phase FAULTS analysis performed while taking these two kinds of domains into account, the observed and calculated profiles were in very good agreement with each other, as can be seen in Figure S6.

kinds of ABC-stacked atomic layers as well as the compounds  $\text{LiMO}_2$  (space group  $R\bar{3}m$ )<sup>10</sup> (M: transition metal). However, 33% of the atoms in the TM layer of  $\text{Li}_2\text{MnO}_3$  are of Li and not of Mn, in contrast to the case for the  $\text{LiMnO}_2$  structure. The Li atoms in the TM layer occupy the  $2b$  sites of  $C2/m$ ; on the other hand, the remaining 67% Mn atoms are located at the  $4g$  sites. These two kinds of atoms form an ordered arrangement in the TM plane (see Figure S-2). The structures were analyzed by the Z-Rietveld code for neutron–synchrotron joint analysis, in order to determine the precise atomic positions and site occupancies of Li, Mn, and Ni first, without considering the stacking faults. The structure refinement results are presented in Table S-II and Figure S-3. Almost all the diffraction peaks were in good agreement with the calculated ones generated using single sets of the profile parameters ( $U$ ,  $V$ , and  $W$  for the synchrotron diffractions and  $\sigma$  and  $\gamma$  for the neutron diffractions).<sup>8</sup> This strongly indicated that the peaks of the synthesized samples were from a single phase of the monoclinic  $\text{Li}_2\text{MnO}_3$  structure, that is, the structure of  $\text{Li}[\text{Li}_{0.2}\text{Mn}_{0.6}\text{Ni}_{0.2}]\text{O}_2$  reported by Jarvis<sup>11</sup> et al., who used the electron diffraction technique to conclude that this material is composed of a solid solution of  $\text{Li}_2\text{MnO}_3$  and  $\text{LiMO}_2$  domains with  $C2/m$  monoclinic symmetry. During the analyses, no atomic mixing between the metal and oxygen layers was assumed; however, all possible metal-atom occupation (mixing) configurations among the  $2c$ ,  $4h$  (both in the Li layer),  $2b$ , and  $4g$  (both in the TM layer) sites were examined, because it is known that the Li and Mn atoms at the  $2b$  and  $4g$  sites show a partially disordered atomic arrangement in  $\text{Li}_2\text{MnO}_3$  (i.e., cation mixing in the TM layer).<sup>2,3,12</sup> These examinations revealed that the Li layers are composed exclusively of Li atoms, whereas the TM layers comprise the atoms of the three metals (Li, Ni, and Mn), which are largely mixed among the  $2b$  and  $4g$  sites. As seen in Table 1, the Mn atoms prefer the  $4g$  site; on the other hand, the Li and Ni atoms tend to selectively occupy the  $2b$  site. This suggests that the  $4g$  site tends to favor the higher-valence cations than does the  $2b$  site. This cation mixing in the TM layers was also confirmed by high-angle annular dark field (HAADF)–scanning transmission electron microscopy (STEM) observations (Figure S-4).

Next, we elucidated the stacking faults in the  $\text{Li}_2(\text{Ni}_x\text{Mn}_{1-x})\text{O}_{3(-\delta)}$  specimens. In the diffraction profiles, fairly intense diffuse peaks related to the stacking faults can be observed, especially at the bottom of the 020, 110, and  $\bar{1}11$  reflections (see Figure 2). This result is similar to that reported for the  $\text{Li}_2\text{MnO}_3$  crystal.<sup>2,3,11–13</sup> The  $\text{Li}_2\text{MnO}_3$  crystal is composed of periodic ABC stacking of three different atomic layers, namely, the TM, O, and Li layers, along the  $c$ -axis direction, as shown below (also see Figure S-2):



Here, this type of layer stacking can be regarded as a structure consisting of ABC stacking of slabs formed by four

**Table 1.** Site Occupancies of the Metal Atoms in the TM Layer of  $\text{Li}_2(\text{Ni}_x\text{Mn}_{1-x})\text{O}_{3(-\delta)}$  ( $x = 0, 1/10, 1/6$ , and  $1/4$ ), As Determined by the Joint Neutron and Synchrotron Analyses

atom	$x = 0$		$x = 1/10$		$x = 1/6$		$x = 1/4$	
	$2b$	$4g$	$2b$	$4g$	$2b$	$4g$	$2b$	$4g$
Li (1)	0.7464	0.1188	0.645	0.131	0.565	0.141	0.500	0.124
Mn (1)	0.2536	0.8812(2)	0.227(1)	0.824	0.261(1)	0.762	0.236(2)	0.716
Ni (1)	–	–	0.127(1)	0.044	0.174(1)	0.097	0.259(1)	0.160

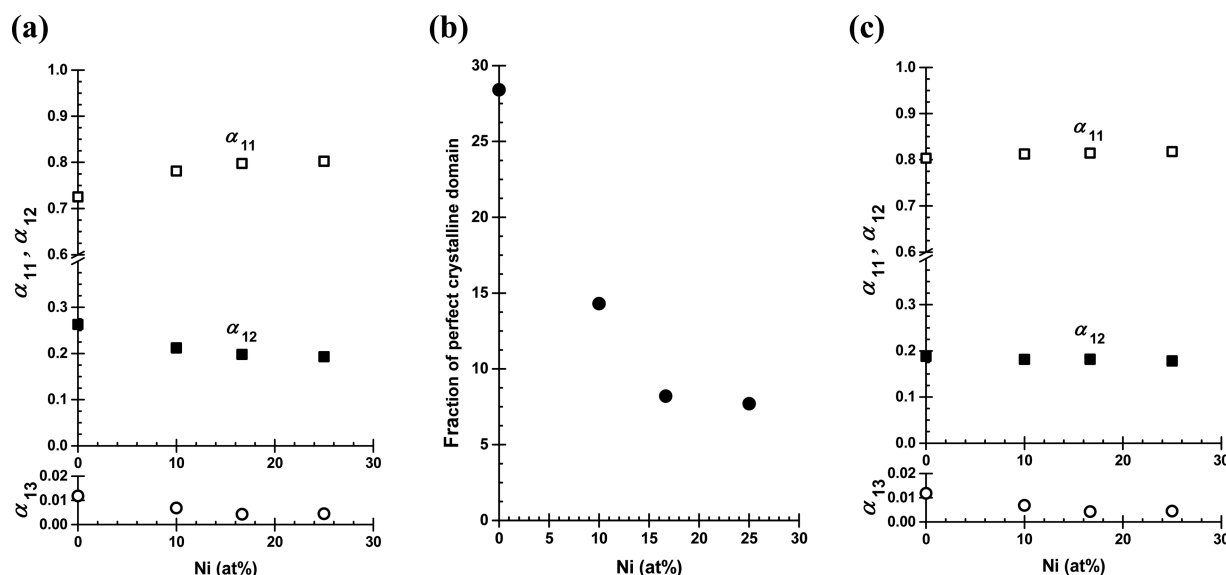


**Figure 3.** (a) Translation probabilities for the three kinds of stacking faults,  $\alpha_{11}$ ,  $\alpha_{12}$ , and  $\alpha_{13}$  and (b) the fractions of the perfect crystalline domains as obtained from the FAULTS analyses for  $\text{Li}_2(\text{Ni}_x\text{Mn}_{1-x})\text{O}_{3(-\delta)}$  ( $x = 0, 1/10, 1/6$ , and  $1/4$ ). (c) The translation probabilities in panel a as averaged (corrected) by the domain fraction shown in panel b. The standard deviations as estimated by the least-squares refinements were smaller than the marks. The labels of the horizontal axes of these graphs show the Ni concentrations,  $x$ , of the  $\text{Li}_2(\text{Ni}_x\text{Mn}_{1-x})\text{O}_{3(-\delta)}$  specimens.

-O-TM-O-Li- atomic layers. Stacking faults are generated in such layered materials by the glide translation of the atomic planes in the  $a$ - $b$  plane. Furthermore, the topologically possible stacking faults can be described fully using three different stacking vectors,  $[0, 0, 1]$ ,  $[1/2, -1/6, 1]$  (both as cubic-type stacking), and  $[1/6, -1/6, 1]$  (as a hexagonal-type stacking), in the monoclinic ( $C2/m$ ) cell (see Figures S-5-1 and S-5-2) and by their combinations (multiplications). During the FAULTS Rietveld refinement process, it was assumed that the stacking faults were allowed only between the interslabs indicated by the arrows and were never generated within the slabs in ill. 1. The probabilities of translation from one slab to the next by these stacking vectors can be represented by the three  $\alpha$  parameters,  $\alpha_{11}$ ,  $\alpha_{12}$ , and  $\alpha_{13}$ . The parameter  $\alpha_{11}$  is the probability for the normal cubic-type stacking found in the perfect  $\text{Li}_2\text{MnO}_3$  crystal, whereas  $\alpha_{12}$  is that for another cubic-type stacking fault related to the ordered atomic arrangement in the TM layers. When  $\alpha_{11} = 1$ ,  $\alpha_{12} = 0$ , and  $\alpha_{13} = 0$ , this crystal has no stacking faults. If the TM layer has a completely disordered (random) atomic arrangement, there is no difference between  $\alpha_{11}$  and  $\alpha_{12}$  (see Figure S-5-2).

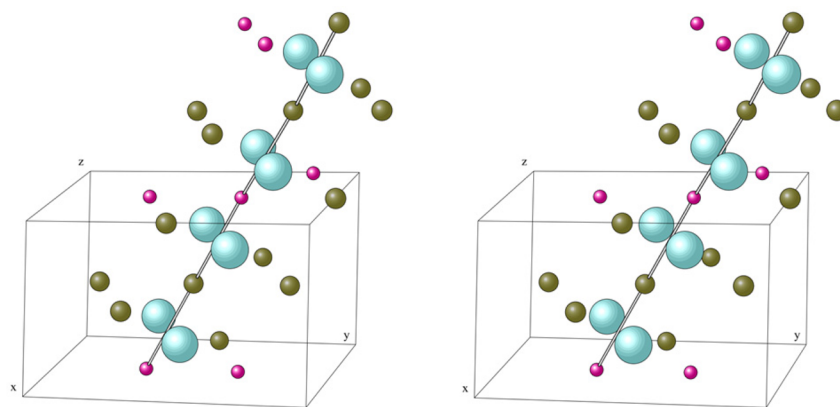
As can be seen in the diffraction patterns (Figure 2), the superstructure reflections consist of sharp and diffuse peaks (see the inset profiles with the backgrounds), which demonstrates that these materials comprise two kinds of domains with different crystallinities. This can be attributed to the existence of highly ordered domains that have perfectly ordered atomic arrangements and no stacking faults as well as disordered domains with the atomic mixing and stacking faults mentioned above, as has been reported for  $\text{Li}_2\text{MnO}_3$ .<sup>2,3,11-13</sup>

Figure 3 shows that the compositional dependencies of parameters  $\alpha_{11}$ ,  $\alpha_{12}$ , and  $\alpha_{13}$  for the imperfect domains, as well as the fraction of perfect (/imperfect) domains as obtained by the FAULTS analysis (the Rietveld analysis results are also shown in Figure S-6). As can be seen in Figure 3a, the  $\alpha_{13}$  parameters, which indicated the formation of hexagonal stacking faults, were almost zero; on the other hand, the cubic stacking faults generated by  $[1/2, -1/6, 1]$  ( $\alpha_{12}$ ) were

20%. These stacking faults in the imperfect domains tended to decrease as the Ni concentration was increased; on the other hand, the fraction of the imperfect domains increased with the increase in the Ni concentration. The volume ratio of the perfect and imperfect domains is shown in Figure 3b. Because the defects in the specimen were diluted by the perfect domains, when applying this average correction to Figure 3a, we could obtain the modified  $\alpha$  parameters, as shown in Figure 3c. As seen in this figure, the  $\text{Li}_2(\text{Ni}_x\text{Mn}_{1-x})\text{O}_{3(-\delta)}$  compounds contain a significant number of stacking faults; however, the average fraction of the stacking faults remains almost unchanged, irrespective of the Ni concentration.

Finally, we show the relationship between the electrochemical behavior and the structural features of the  $\text{Li}_2(\text{Ni}_x\text{Mn}_{1-x})\text{O}_{3(-\delta)}$  specimens. Pure  $\text{Li}_2\text{MnO}_3$  does not show any property, because manganese is only at a +4 state in this material. It is simply expected that, as soon as Ni is introduced in the material, redox can occur and electrochemical properties are improved. However, in the case of the  $\text{Li}_2(\text{Ni}_x\text{Mn}_{1-x})\text{O}_{3(-\delta)}$  crystals, it is essential that the Li ions in the TM layers are used as effectively as those in the Li layers, in order to ensure superior electrochemical performance; in other words, the Li ions need to smoothly migrate within as well as across the layers during the charging–discharging processes (see section 1 in the Supporting Information). In these crystals, every metal atom in the Li and TM layers has 12 metal (Li or Mn/Ni) atoms as the second nearest neighbors (see Figures S-2 and S-7). When the Li ions jump into the positions of their 12 neighboring metal atoms, they have to pass through the potential barrier formed by the six obstructing atoms (two O ions and four Li/Mn ions) located around each jumping axis (see Figures 4 and S-8). In a perfect crystal, when a conducting Li ion moves continuously to the neighboring Li positions, it necessarily encounters the potential barrier formed by the contribution of one or two Mn/Ni ions, as seen in Figures 4 and S-8, within two jumping steps. Of the Li, Mn, Ni, and O obstructing atoms, the Mn atoms make it the most difficult for the migrating Li atoms to slip through the barriers; this is because they are tetravalent





**Figure 4.** Stereo graphic of a Li–Mn chain (connected by bars) and the obstructing atoms located along the chain in a perfectly ordered  $\text{Li}_2\text{MnO}_3$  crystal (cross-eyed stereo viewing: Li, dark green; O, aqua; and Mn, pink). This chain can be a smooth Li percolation path in the  $\text{Li}_2(\text{Ni}_x\text{Mn}_{1-x})\text{O}_{3(-\delta)}$  crystal as well (even along the  $c$ -axis direction, as shown in this figure), when the Mn/Ni atoms in the chain are replaced by Li atoms and the obstructing  $\text{Mn}^{4+}$  ions are substituted by  $\text{Li}^+$  or  $\text{Ni}^{2+}$  ions (Figure S-8 shows other examples).

cations ( $\text{Mn}^{4+}$ ), forming a significantly large Coulomb potential so as to cut off the paths.<sup>14</sup> Then, when these  $\text{Mn}^{4+}$  ions are replaced by low-valence cations such as  $\text{Li}^+$  or  $\text{Ni}^{2+}$ , it is expected that the conducting Li ions can move to the neighboring positions more easily.

The significant number of stacking faults and cation mixing in  $\text{Li}_2(\text{Ni}_x\text{Mn}_{1-x})\text{O}_{3(-\delta)}$  can cause an exchange of the  $\text{Mn}^{4+}/\text{Ni}^{2+}$  and  $\text{Li}^+$  positions in the TM layer. Figures 4 and S-8 show several of an enormous number of metal-atom chains in the  $\text{Li}_2(\text{Ni}_x\text{Mn}_{1-x})\text{O}_{3(-\delta)}$  crystals. When the transition metals on the chain in Figure 4 are replaced by Li atoms, this chain acts as a Li-percolation path; when the obstructing high-valence  $\text{Mn}^{4+}$  cations around the chains in Figures 4 and S-8 are replaced by low-valence cations ( $\text{Li}^+$  or  $\text{Ni}^{2+}$ ), these chains become smoother Li percolation paths. In the synthesized  $\text{Li}_2(\text{Ni}_x\text{Mn}_{1-x})\text{O}_{3(-\delta)}$  specimens, as the Ni content was increased, the number of lower-valence Ni ions increased instead of the number of the higher-valence Mn ions. Furthermore, the degree of atomic mixing became more significant (see Table 1). These phenomena resulted in an increase in the number of longer and smoother percolation paths. It is, therefore, deemed that the replacement of Mn with Ni results in active Li ions and increases the charge-discharge capacity (see Figure 1). In other words, the idea of Lee<sup>14</sup> et al. of facilitating smooth Li percolation is topologically realized in the  $\text{Li}_2(\text{Ni}_x\text{Mn}_{1-x})\text{O}_{3(-\delta)}$  compounds, and we believe that the interchanging of the atomic positions of Li and Mn/Ni is one of the major reasons for the compounds exhibiting performances better than that of  $\text{Li}_2\text{MnO}_3$  (also see section 2 in the Supporting Information).

## EXPERIMENTAL METHODS

$\text{Li}_2(\text{Ni}_x\text{Mn}_{1-x})\text{O}_{3(-\delta)}$  ( $x = 0, 1/20, 1/10, 1/6$ , and  $1/4$ ) were synthesized by a solid-state reaction of  $\text{LiOH}\cdot\text{H}_2\text{O}$ ,  $\text{NiCO}_3$ , and  $\text{MnCO}_3$  at a molar ratio of 2.1:  $x$ :  $1 - x$  as precursors. These starting materials were thoroughly mixed by milling in acetone for 2 h and then dried at 100 °C. The precursors were pelletized at 5 MPa and calcined at 450 °C for 24 h. They were powdered and pressed again to form new pellets, which were then annealed at 900 °C for 12 h in the air. The heating and cooling rates were both 300 °C h<sup>-1</sup>.

A mixture of the active material, acetylene black (Denki Kagaku Kogyo), and polyvinylidene difluoride (PVDF, Kureha) with a weight ratio of 80:10:10 was spread onto an aluminum

foil with 1-methyl-2-pyrrolidone (NMP) and then dried at 80 °C under vacuum overnight to constitute a positive electrode. The electrode was pressed to a typical thickness of 30–35  $\mu\text{m}$ . Metallic lithium foil (0.2 mm in thickness, > 99.9%, Honjo Metal) was used as counter and reference electrodes. These components were assembled together with the s polyolefin separator and soaked in the electrolyte solution in an Ar-filled glovebox, which were sealed in an aluminum-coated laminate-type cell. The electrolyte used in this study was 1 M  $\text{LiPF}_6$ , which was dissolved in anhydrous ethylene carbonate (EC) and ethyl methyl carbonate (EMC) with a volumetric ratio of 3:7 (Kishida Chemical). The electrochemical measurements were performed at room temperature on an automatic cycling and data recording system (HJ1001SD8, Hokuto Denko).

Synchrotron diffraction experiments were performed using a large-diameter Debye–Scherrer camera with an imaging plate on the BL02B2 beamline at the Japan Synchrotron Radiation Research Institute (JASRI/SPring-8).<sup>15</sup> The neutron powder diffraction data were obtained using a time-of-flight powder diffractometer (BL09 beamline, SPICA) at the Japanese Proton Accelerator Research Complex (J-PARC).<sup>16</sup> Inductively coupled plasma atomic emission spectroscopy (for metals) and iodometric redox titration (for oxygen) analyses were used to determine the compositions of the synthesized products (Table S-1).

## ASSOCIATED CONTENT

### Supporting Information

The Supporting Information is available free of charge on the ACS Publications website at DOI: 10.1021/acs.jpclett.6b00587.

Additional discussion, tables, and figures (PDF)

## AUTHOR INFORMATION

### Corresponding Author

\*E-mail: t-matsunaga@rising.saci.kyoto-u.ac.jp. Tel: +81-774-38-4969. Fax: +81-774-38-4996.

### Notes

The authors declare no competing financial interest.

## ACKNOWLEDGMENTS

This work was supported by the Research and Development Initiative for Scientific Innovation of New Generation Batteries (RISING) project of the New Energy and Industrial

Technology Development Organization (NEDO), Japan. The authors thank Prof. Yukinori Koyama at Kyoto University for his fruitful suggestions and Mr T. Kakei, Mr Y. Kamishima, and Dr. Y. Takabayashi for their experimental support. The TOC graphic was prepared using VESTA,<sup>17</sup> and the other structure models were displayed by using Java Structure Viewer (JSV 1.08 lite), which was created by Dr. Steffen Weber. The synchrotron radiation experiments were performed with the approval of JASRI/SPRING-8 (Proposals 2015A1013 and 2015B1014). The authors are grateful to Dr K. Sugimoto and Dr S. Kawaguchi for their kind support. The neutron diffraction experiments were conducted as part of the S-type project of the High Energy Accelerator Research Organization (KEK) (Proposal 2014S10).

## REFERENCES

- (1) Yu, D. Y. W.; Yanagida, K.; Kato, Y.; Nakamura, H. Electrochemical Activities in  $\text{Li}_2\text{MnO}_3$ . *J. Electrochem. Soc.* **2009**, *156*, A417–A424.
- (2) Boulineau, A.; Croguennec, L.; Delmas, C.; Weill, F. Structure of  $\text{Li}_2\text{MnO}_3$  with Different Degrees of Defects. *Solid State Ionics* **2010**, *180*, 1652–1659.
- (3) Matsunaga, T.; Komatsu, H.; Shimoda, K.; Minato, T.; Yonemura, M.; Kamiyama, T.; Kobayashi, S.; Kato, T.; Hirayama, T.; Ikuhara, Y. et al. Synthesis Temperature Dependence of Structural Defects in  $\text{Li}_2\text{MnO}_3$ . *Chem. Mater.*, submitted for publication, **2016**.
- (4) Lu, Z.; Beaulieu, L. Y.; Donabarger, R. A.; Thomas, C. L.; Dahn, J. R. Synthesis, Structure, and Electrochemical Behavior of  $\text{Li}[\text{Ni}_x\text{Li}_{1/3-2x/3}\text{Mn}_{2/3-x/3}]\text{O}_2$ . *J. Electrochem. Soc.* **2002**, *149*, A778–A791.
- (5) Song, B.; Liu, H.; Liu, Z.; Xiao, P.; Lai, M. O.; Lu, L. High Rate Capability Caused by Surface Cubic Spinel in Li-rich Layer-structured Cathodes for Li-ion Batteries. *Sci. Rep.* **2013**, *3*, 3094.
- (6) Casas-Cabanas, M.; Rodríguez-Carvajal, J.; Palacín, M. R. FAULTS, a New Program for Refinement of Powder Diffraction Patterns from Layered Structures. *Z. Kristallogr. Suppl.* **2006**, *2006*, 243–248.
- (7) Treacy, M. M. J.; Newsam, J. M.; Deem, M. W. A General Recursion Method for Calculating Diffracted Intensities from Crystals Containing Planar Faults. *Proc. R. Soc. London, Ser. A* **1991**, *433*, 499–520.
- (8) Oishi, R.; Yonemura, M.; Nishimaki, Y.; Torii, S.; Hoshikawa, A.; Ishigaki, T.; Morishima, T.; Mori, K.; Kamiyama, T. Rietveld Analysis Software for J-PARC. *Nucl. Instrum. Methods Phys. Res., Sect. A* **2009**, *600*, 94–96.
- (9) Boulineau, A.; Croguennec, L.; Delmas, C.; Weill, F. Reinvestigation of  $\text{Li}_2\text{MnO}_3$  Structure: Electron Diffraction and High Resolution TEM. *Chem. Mater.* **2009**, *21*, 4216–4222.
- (10) Strobel, P.; Lambert-Andron, B. Crystallographic and Magnetic Structure of  $\text{Li}_2\text{MnO}_3$ . *J. Solid State Chem.* **1988**, *75*, 90–98.
- (11) Jarvis, K. A.; Deng, Z.; Allard, L. F.; Manthiram, A.; Ferreira, P. J. Atomic Structure of a Lithium-Rich Layered Oxide Material for Lithium-Ion Batteries: Evidence of a Solid Solution. *Chem. Mater.* **2011**, *23*, 3614–3621.
- (12) Kubota, K.; Kaneko, T.; Hirayama, M.; Yonemura, M.; Imanari, Y.; Nakane, K.; Kanno, R. Direct Synthesis of Oxygen-deficient  $\text{Li}_2\text{MnO}_{3-x}$  for High Capacity Lithium Battery Electrodes. *J. Power Sources* **2012**, *216*, 249–255.
- (13) Lei, C. H.; Wen, J. G.; Sardela, M.; Bareño, J.; Petrov, I.; Kang, S.-H.; Abraham, D. P. Structural Study of  $\text{Li}_2\text{MnO}_3$  by electron Microscopy. *J. Mater. Sci.* **2009**, *44*, 5579–5587.
- (14) Lee, J.; Urban, A.; Li, X.; Su, D.; Hautier, G.; Ceder, G. Unlocking the Potential of Cation-disordered Oxides for Rechargeable Lithium Batteries. *Science* **2014**, *343*, 519–522.
- (15) Nishibori, E.; Takata, M.; Kato, K.; Sakata, M.; Kubota, Y.; Aoyagi, S.; Kuroiwa, Y.; Yamakata, M.; Ikeda, N. The Large Debye-Scherrer Camera Installed at Spring-8 BL02B2 for Charge Density Studies. *J. Phys. Chem. Solids* **2001**, *62*, 2095–2098.
- (16) Yonemura, M.; Mori, K.; Kamiyama, T.; Fukunaga, T.; Torii, S.; Nagao, M.; Ishikawa, Y.; Onodera, Y.; Adipranoto, D. S.; Arai, H.; et al. Development of SPICA, New Dedicated Neutron Powder Diffractometer for Battery Studies. *J. Phys.: Conf. Ser.* **2014**, *502*, 012053.
- (17) Momma, K.; Izumi, F. VESTA 3 for Three-dimensional Visualization of Crystal, Volumetric and Morphology Data. *J. Appl. Crystallogr.* **2011**, *44*, 1272–1276.